nature communications

Article

https://doi.org/10.1038/s41467-025-64318-w

Dynamic identification of reactive iron-oxo species in heterogeneous fenton-like reaction via operando stopped-flow IR spectroscopy

Received: 9 December 2024

Accepted: 13 September 2025

Published online: 17 October 2025

Check for updates

Qi Zhao[1,2,3], Qiang Huang[1,2,3], Ran Duan[1], Zhiyong Zhang[1,2], Yangen Xie[1,2], Wenjing Song[1,2], Hua Sheng[1,2] ✉ & Jincai Zhao[1,2]

Heterogeneous high-valent iron-oxo species ($Fe^{IV}=O$) are known as reactive oxygen species with specific oxygen-atom transfer capabilities, yet the characterization of their presence and kinetic behaviors in Fenton or Fenton-like systems remains challenging under conventional techniques. Herein we develope a operando technique through the integration of the stopped-flow (SF) technique with rapid-scan attenuated total reflection (ATR) IR spectroscopy. This operando technique allows for dynamic monitoring of heterogeneous Fenton reactions, including the variations and kinetics of reactants and intermediates with a maximum time resolution of 60 ms. Supported by this technique, our investigation of the peroxymonosulfate (PMS)-based Fenton-like reaction on an Fe-N_4 single-atom catalyst (Fe-N-C) not only confirms the formation of surface $Fe^{IV}=O$ but also provides the experimental identification of its lifetime on the timescale of seconds (3.96 s) through spectral kinetics analysis. Additionally, we uncover an oxygen exchange between $Fe^{IV}=O$ and water molecules, further substantiating the notion of $Fe^{IV}=O$ as a long-lived reactive species in aqueous systems. Furthermore, based on the spectroscopic results, leveraging the specific reactivity of $Fe^{IV}=O$ towards aqueous As^{III} along with its extended lifetime, we achieve effective preferential removal of As^{III} even in complex wastewater environments using Fe-N-C/PMS system.

Fenton and Fenton-like reactions, as advanced oxidation processes (AOPs), are widely recognized for their effectiveness in removing environmental pollutants and degrading recalcitrant organic matter in water and soil[1–4]. The activity of Fenton or Fenton-like reactions arises from the activation of peroxides such as H_2O_2, peroxymonosulfate (PMS) and peroxydisulfate (PDS), which generate reactive oxygen species (ROS), including •OH, $O_2^{\bullet-}$, $SO_4^{\bullet-}$, $SO_5^{\bullet-}$, and $^1O_2$[5–9]. Most ROS generated are radicals released from the surface of Fenton catalysts, initiating homogeneous oxidative reactions with the pollutants. In contrast, the high-valent metal-oxo species (e.g., $Fe^{IV}=O$[10–12], $Co^{IV}=O$[13]) display distinct behaviors in oxidation processes compared to radicals, as they typically engage in two-electron oxygen atom transfer (OAT) processes[14], whereas radicals favor single-electron oxidation pathways. This pathway is particularly efficient in processes such as water

[1]Key Laboratory of Photochemistry, Institute of Chemistry, Chinese Academy of Sciences, Beijing National Laboratory for Molecular Sciences, Beijing, PR China. [2]University of Chinese Academy of Sciences, Beijing, PR China. [3]These authors contributed equally: Qi Zhao, Qiang Huang.
✉e-mail: hsheng@iccas.ac.cn

oxidation[15], epoxidation[16], alkane hydroxylation[17], and the oxidation of sulfides/phosphides[18,19], decreasing energy barriers and avoiding side reactions. Additionally, since metal-oxo species are surface-bound, their reaction dynamics significantly differ from the homogeneous reactions of other ROS. However, compared to radicals or $^1O_2$ with state-of-the-art techniques, such as electron paramagnetic resonance (EPR) spectroscopy, to characterize their appearance in the reactions, metal-oxo species remain somewhat elusive, possibly due to their surface-bound nature; these typical techniques applicable for homogeneous radicals are ineffective for the detection of metal-oxo. As a result, the existence of metal-oxo species and their roles in pollutant degradation, particularly in heterogeneous Fenton or Fenton-like systems, is still a subject of debate[20].

Currently, approaches for identifying metal-oxo species can be broadly categorized into two main strategies: the use of molecular probes[21–24] and direct detection via vibrational spectroscopy techniques, such as ATR-FTIR and resonance Raman Spectroscopy[24–27]. Each method presents inherent challenges in terms of sensitivity, selectivity, and the transient nature of reactive intermediates. In the first category, methyl phenyl sulfoxide (PMSO) is commonly employed, with metal-oxo species believed to oxidize PMSO directly to methyl phenyl sulfone ($PMSO_2$) via oxygen-atom transfer. While the formation of $PMSO_2$ is often cited as evidence for the presence of metal-oxo, this method is not entirely conclusive, as other oxidizing agents can also convert PMSO to $PMSO_2$ under certain conditions[28]. Vibrational spectroscopy is another approach used to detect metal-oxo species, though it has limitations. For example, Mössbauer spectroscopy requires a very low temperature to detect Fe-oxo, which may not reflect actual reaction conditions. Techniques like infrared or Raman spectroscopy often exhibit low sensitivity to metal-oxo species. Furthermore, to date, the spectroscopic identification of metal-oxo in various systems—whether enzyme-like, photoelectrochemical, or Fenton—has been largely qualitative, aiming only to confirm the presence of the intermediate[4,10–13,23]. These spectroscopic techniques are typically steady-state, meaning they cannot provide real-time kinetics information about the formation and depletion of metal-oxo, and are incapable of tracking its life cycle. The long intervals between steady-state spectral collections also introduce baseline variations, obscuring the weak signals of metal-oxo.

To achieve time-dependent spectroscopy monitoring, it is crucial to precisely synchronize the reaction timeline with the spectra collection process. In other words, the starting points of the reaction and spectral data collection must align accurately. In the case of the Fenton reaction, which is initiated by mixing peroxide with a Fenton catalyst, employing the stopped-flow technique in conjunction with rapid-scan spectroscopy offers a potential solution. However, the classical stopped-flow technique is designed for homogeneous systems, facilitating the rapid mixing of two liquid-phase reactants and the synchronized monitoring of real-time changes in reagents, intermediates, and products via UV-visible spectroscopy[29]. To date, the application of the stopped-flow technique in heterogeneous systems alongside vibrational spectroscopy has not been reported.

Herein, we employ an adapted Stopped-Flow technique in conjunction with rapid-scan attenuated total reflection (ATR) Infrared spectroscopy, enabling in-situ monitoring of the heterogeneous Fenton reactions with a maximum time resolution of 60 ms. Supported by this technique, our investigation of the PMS-based Fenton-like reaction on a Fe-N_4 single-atom catalyst (Fe-N-C) not only confirms the presence of surface $Fe^{IV}=O$ but also provides the experimental identification of its lifetime on the timescale of seconds (3.96 s) through spectral kinetics analysis. Additionally, we uncover an oxygen exchange between $Fe^{IV}=O$ and water molecules, further substantiating the notion of $Fe^{IV}=O$ as a long-lived reactive species in aqueous systems. This innovative in-situ technique offers an approach to elucidate reaction pathways in Fenton reactions and can be applied to other reactions initiated by mixing reactants. Furthermore, based on the spectroscopic results, leveraging the specific reactivity of $Fe^{IV}=O$ towards aqueous As^{III} along with its extended lifetime, we achieve effective preferential removal of As^{III} even in complex wastewater environments using the Fe-N-C/PMS system.

Results

Methodology of rapid-scan ATR-IR spectroscopy in conjunction with Stopped-Flow technique (SF-ATR-IR)

To enable real-time monitoring of the heterogeneous Fenton reaction, an approach coupling in situ IR technique with an adapted stopped-flow method is developed. The conventional stopped-flow technique is a rapid mixing method developed for homogeneous reactions. In this method, two or more reactants are quickly mixed in an observation chamber, and the flow is then abruptly stopped to allow the detector to monitor the reaction kinetics starting from the moment of mixing. However, this typical setup is not suitable for heterogeneous reactions. Here, we adopted the concept of "stopped-flow" but modified it to accommodate the nature of the heterogeneous Fenton-like reaction, where the reaction is initiated by the contact between the Fenton catalyst and PMS (or PDS).

To enable surface-specific monitoring, we first deposited the Fenton catalyst onto an ATR diamond crystal by evacuating the catalyst suspension (Fig. 1 and Supplementary Fig. 1), which serves as a role analogous to the observation chamber in the conventional setup. Given that the detection depth of ATR-IR is limited to just a few micrometers above the crystal surface, only reactions occurring on the deposited catalyst layer are detected. Therefore, the catalyst film

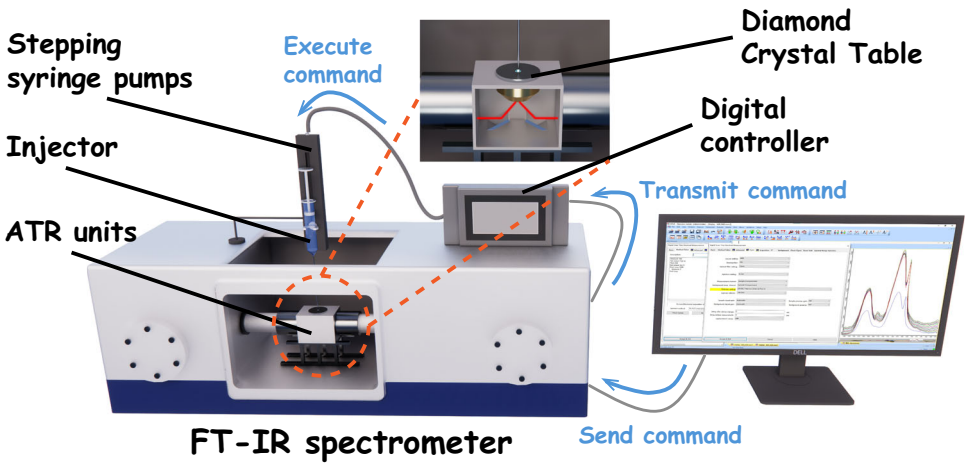

Fig. 1 | Schematic diagram of the instrument. The instrumental setup for rapid-scan SF-ATR-FTIR spectroscopy.

thickness is controlled within 1–2 μm to ensure effective signal capture (Supplementary Fig. 2a, b). On the other hand, a digitally controlled stepping syringe pump was utilized to precisely inject PMS or PDS solutions. We then used a syringe pump to inject the PMS solution, abruptly stopping it at the catalyst-coated surface, ensuring that only the surface reaction is "observed". This modified stopped-flow configuration allows us to selectively track the interfacial reaction between PMS and the catalyst in real-time.

Prior to PMS/PDS injection, 10 μL of distilled water was added to the catalyst membrane. This serves a dual purpose: it acts as a buffer layer for the PMS/PDS drops and mitigates baseline variations in the IR spectrum, which could arise from the transition between a gas-solid interface and a water-solid interface when PMS/PDS is applied directly to the dry catalyst membrane. Upon injection of a drop of PMS/PDS (approximately 10 μL), the PMS/PDS molecules diffuse through the buffer layer, abruptly "stopping" at the catalyst membrane's surface to initiate the Fenton-like reaction and ensure that only the surface reaction is "observed".

The operation of the syringe pump is synchronized with the IR spectrometer, triggering the injection of PMS/PDS in response to the forward movement of the spectrometer's mirror. Consequently, IR data acquisition begins simultaneously with the PMS/PDS injection from the syringe. The data collection occurs in rapid-scan mode, capturing IR spectra with a maximum time resolution of 60 ms per spectrum. Importantly, the ATR-IR technique only detects signals within 1–2 μm above the ATR crystal surface[30]; therefore, only when PMS/PDS molecules diffuse close to the catalyst membrane can they be observed in the IR spectra. This SF-ATR-FTIR technique thus provides valuable insights specifically focused on the surface reactions between PMS/PDS and Fenton catalysts.

Noteworthy, to observe the weak IR signals of Fe-oxo and peroxide intermediates, the operating conditions of ATR-IR are carefully optimized. The use of an oxidation-resistant diamond crystal prevents Fe-oxo species from reacting with the ATR crystal. Additionally, the use of a mid-band MCT detector, with a cutoff at 625 cm^{-1}, enhances sensitivity for detecting the low-frequency Fe-oxo band. The entire IR spectroscopy sample chamber is continuously purged with dry argon to minimize atmospheric water vapor interference and improve the signal-to-noise ratio (Supplementary Fig. 2c). All of these optimizations, combined with the flexibility to introduce various catalysts and reagents, make this technique applicable to a wide range of reaction types—whether heterogeneous or homogeneous—including mixing-triggered reactions such as the Fenton reaction, enzyme catalysis, and catalytic organic synthesis.

Preparation and Characterization of Fe-N-C Catalyst

To validate the capability of our spectroscopy technique for dynamically identifying heterogeneous metal-oxo species, we conducted a study using Fe-N-C, a single-atom catalyst with Fe-N_4 coordination. Single-atom Fe-N-C catalysts have attracted significant attention in energy- and environment-related applications and have recently emerged as promising Fenton catalysts[31]. These catalysts are typically fabricated by stabilizing monodispersed metal atoms on nitrogen-doped carbon substrates (M-N-C) through nitrogen-coordination (MN_x)[32]. This approach allows for precise tuning of the MN_x structure to control the types of reactive species generated during Fenton or Fenton-like processes. Of particular interest is the possible formation of metal-oxo species on M-N-C catalysts, as suggested by prior studies employing PMSO-probe experiments[23,33,34]. The formation of surface metal-oxo on single-atom catalysts would offer additional advantages: on conventional catalysts with adjacent metal sites, the synergistic interaction between two adjacent metal-oxo species makes them prone to rapid consumption through reaction with water, limiting their effective utilization in pollutant removal. In contrast, the isolated nature of metal sites in single-atom catalysts prevents such undesirable interactions, effectively shielding the metal-oxo species from premature decay. This extends the lifetime of metal-oxo species, allowing them to serve as more efficient oxidants for pollutant removal rather than being wasted in reactions with the aqueous matrix. Therefore, exploring the formation and dynamic kinetics of metal-oxo species on single-atom catalysts holds profound significance.

The typical single-atom Fe catalyst was synthesized via an adapted method from literature[22,35]: the $Fe(Phen)_3$ precursors were first templated by nano-MgO, followed by calcination under argon gas and removal of templates by nitric acid leaching to obtain Fe-N-C (Fig. 2a). Scanning electron microscopy (SEM) images revealed that the resulting Fe-N-C featured a pleated and porous structure (Supplementary Fig. 3), while energy-dispersive X-ray spectroscopy (EDS) mapping confirmed the uniform distribution of Fe, N, and C elements (Fig. 2b). X-ray diffraction (XRD) analysis showed no diffraction peaks corresponding to crystalline or aggregated Fe (Supplementary Fig. 4). High-angle annular dark-field scanning transmission electron microscopy (HAADF-STEM) images further verified that Fe atoms were atomically dispersed across the carbon matrix without signs of clustering (Fig. 2c, d). This evidence underscored the effective synthesis of single-atom Fe catalysts with uniform dispersion.

The chemical state of Fe was analyzed using X-ray photoelectron spectroscopy (XPS). The high-resolution Fe *2p* spectrum revealed that Fe primarily exists in the Fe^{II} state, with a peak-area ratio of 61.6% (Supplementary Fig. 5). Additionally, the N *1s* spectrum displayed an Fe-N peak at 399.13 eV, confirming the presence of Fe in the N-coordinated Fe-N_x form[36]. The K-edge X-ray absorption near-edge structure (XANES) spectrum of Fe showed that the absorption edge of Fe-N-C closely aligns with that of standard iron phthalocyanine (FePc), indicating a predominant Fe^{2+} oxidation state, consistent with the XPS findings (Fig. 2e). Extended X-ray absorption fine structure (EXAFS) spectroscopy was utilized to probe the coordination environment of Fe in Fe-N-C. The spectrum exhibited a prominent peak at ~1.5 Å, corresponding to the Fe-N first coordination shell. Notably, the absence of Fe-Fe peaks at ~2.2 Å (metallic Fe) or ~2.7 Å (Fe-Fe in FeO_x) further validated the atomic dispersion of Fe within the Fe-N-C matrix[37] (Fig. 2f). The EXAFS wavelet transformation of Fe-N-C displayed a maximum intensity at ~4.0 $Å^{-1}$, associated with the Fe-N interaction (Supplementary Fig. 6), confirming the atomically dispersed nature of Fe without detectable crystalline metallic phases. Finally, curve-fitting analysis of the EXAFS data indicated an Fe-N_4 coordination number of approximately 3.8 (Supplementary Fig. 7, Supplementary Table 1), affirming the presence of the Fe-N_4 structure.

The dynamic spectroscopic identification of $Fe^{IV}=O$ in the Fenton-like reaction between Fe-N-C and PMS

The active species generated during the Fenton-like reaction between Fe-N-C and PMS was monitored in situ using SF-ATR-FTIR. As discussed above and shown in Fig. 3a, due to the detecting scope of ATR-IR that is limited to the near-surface region of the ATR crystal (or deposited catalyst membrane), there is an inherent delay between the injection of PMS and the observation of PMS or its reaction intermediates in the IR spectra, arising from the time required for PMS to diffuse from the syringe pump to the ATR crystal. To estimate this diffusion duration, we first conducted a controlled experiment on a bare diamond ATR crystal.

Noteworthy, the commercially available PMS is not solely a purified sample of potassium hydrogen persulfate ($KHSO_5$); it also contains redox-inert $KHSO_4$ and K_2SO_4. Therefore, we need to identify characteristic IR bands for each component to separately estimate their near-surface concentrations. These characteristic bands should be distinct and not overlap with those of other components. As shown in Supplementary Fig. 8a, the standard IR spectrum of the PMS mixture reveals several distinct bands. Notably, the characteristic IR bands for persulfates appear at 1250 and 1060 cm^{-1}, corresponding to the S-O

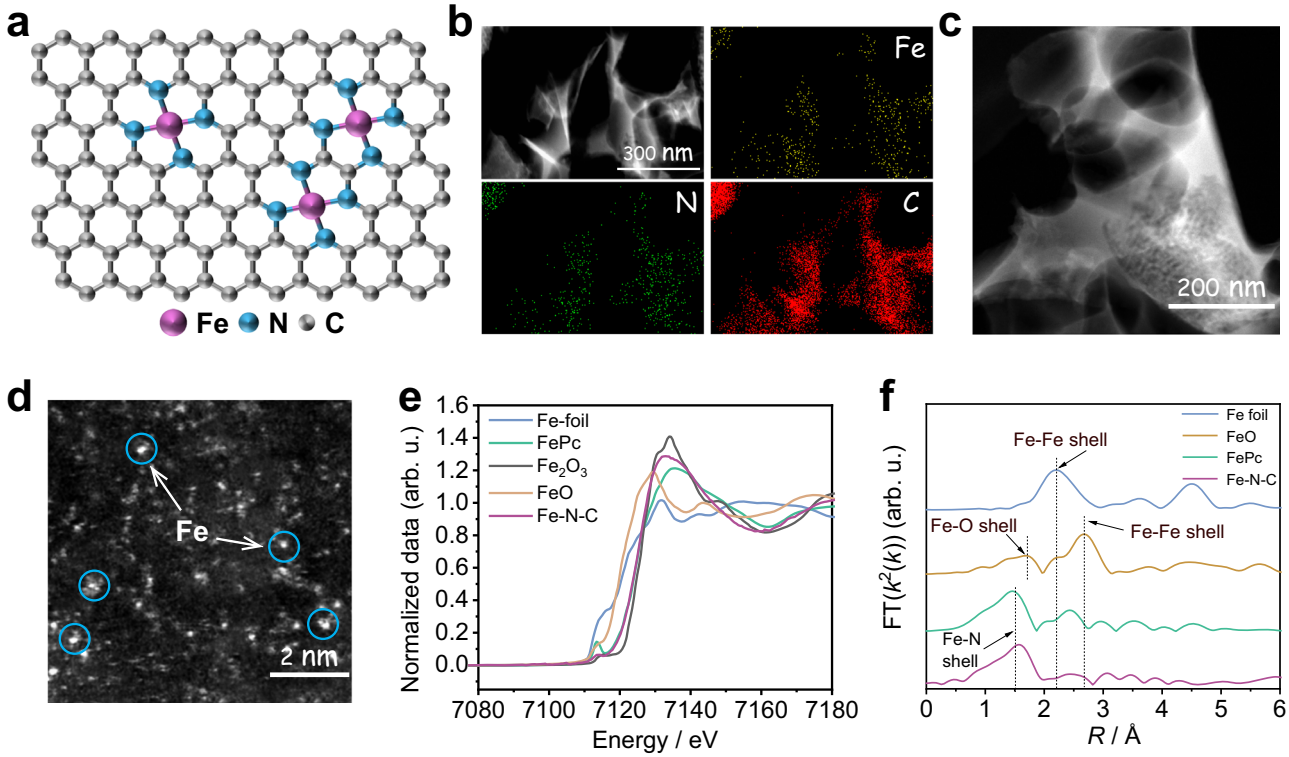

Fig. 2 | Structural and spectroscopic characterization of single-atom catalyst Fe-N-C. a Schematic illustration of the chemical structure of Fe-N-C. **b** Energy-dispersive X-ray spectroscopy (EDS) mapping images. **c** Transmission electron microscopy (TEM) image and **d** High-angle annular dark-field scanning transmission electron microscopy (HAADF-STEM) image of Fe-N-C. (Blue circles highlight a portion of Fe single atoms) **e** Normalized Fe K-edge X-ray absorption near-edge structure (XANES) spectra and **f** Fourier-transformed extended X-ray absorption fine structure (FT-EXAFS) spectra of Fe-N-C, Fe_2O_3, FePc (iron phthalocyanine), FeO and Fe foil. Source data for Fig. 2e, f are provided as a Source Data file.

(or S = O) vibrations of the SO_3 moiety, as well as the peroxyl (O-O) bond at 880 cm^{-1}. For the other two components, $KHSO_4$ exhibits IR bands at 1193 and 1050 cm^{-1}, while K_2SO_4 shows a band at 1100 cm^{-1}. To avoid interference among the components, we used the intensity of the 1250, 1193 and 1100 cm^{-1} bands to represent HSO_5^-, HSO_4^- and SO_4^{2-}, respectively.

On the bare diamond ATR crystal, as illustrated in Fig. 3b, the IR bands corresponding to HSO_5^-, HSO_4^- and SO_4^{2-}, became detectable 0.6 s after syringe injection. The kinetics of all PMS components showed a similar pattern (Fig. 3d and Supplementary Fig. 8b, solid symbols): their intensities sharply increased until stabilizing around 18.0 s, indicating that PMS diffusion had reached equilibrium. However, when Fe-N-C was deposited on the diamond crystal, as shown in Fig. 3c and d (empty symbols), the observation delay for the HSO_5^- band at 1250 cm^{-1} extended by an additional 0.5 s. Following this delay, the increase in intensity was slower. Notably, after peaking at 12.0 s, the intensity began to decline and was completely depleted at approximately 100.0 s. This behavior suggested that HSO_5^- was actively reacting with the Fe-N-C catalyst, with the apparent intensity of the 1250 cm^{-1} band reflecting the difference between HSO_5^- that diffused to the surface and that consumed in the reaction. In contrast, the intensities of HSO_4^- and SO_4^{2-} exhibited a monotonic increase, reaching higher equilibrium values than on the bare diamond. This accelerated increase was attributed to the generation of HSO_4^- and SO_4^{2-} from the reaction between HSO_5^- and the Fe-N-C catalyst.

Significantly, almost concurrently with the appearance of the HSO_5^- band, a new band at 833 cm^{-1} emerged (Fig. 3c), closely matching the frequency of surface $Fe^{IV}=O$ reported in the literature[38]. As shown in the kinetics (Fig. 3e, f), the IR bands of HSO_5^- (1250 cm^{-1}) began to decay at approximately 12 s, marking the point where the consumption of near-surface HSO_5^- outpaced its supplement from the bulk solution. Complete depletion of the 1250 cm^{-1} band was observed at 230.16 s, suggesting the exhaustion of HSO_5^- in both the near-surface region and the bulk system. In contrast, the 833 cm^{-1} band exhibited a delayed decay, initiating at approximately 66 s, with complete disappearance occurring at 234.12 s (Fig. 3e, f). The extended existence of $Fe^{IV}=O$, lasting an additional 3.96 s beyond the depletion of HSO_5^-, highlights its long lifetime on the Fe-N-C on the scale of seconds. This result provided the experimental identification of the lifetime of surface metal-oxo generated during the Fenton reaction.

The effect of pH on the lifetime of $Fe^{IV}=O$ was also examined, given that $Fe^{IV}=O$ can degrade via reaction with H^+ to form Fe^{III}. As shown in Supplementary Fig. 8c–e, adjusting the pH of the Fenton-like system from approximately 2 (the original value used in the above experiments) to 7 using NaOH led to a slight increase in the $Fe^{IV}=O$ lifetime from 3.96 s to 4.08 s, an increase of only 0.12 s, about 3% of the original lifetime. This indicates that although $Fe^{IV}=O$ is slightly more stable under neutral conditions, the overall extension is minimal, suggesting that pH has a limited impact on its lifetime (Supplementary Fig. 8c–e).

To further consolidate the assignment of the IR band corresponding to surface $Fe^{IV}=O$ on Fe-N-C, we conducted an ^{18}O isotope labeling experiment. Due to the lack of commercially available ^{18}O-labeled persulfate, we opted to use ^{18}O-labeled water ($H_2{}^{18}O$) instead. Since surface $Fe^{IV}=O$ is produced from the oxidation of persulfate, it implies that the oxo O originates from persulfate rather than water. Consequently, the ^{18}O labeling of water should have a minimal impact on the source of the oxo groups. However, previous studies have indicated that an oxygen exchange can occur between $Fe^{IV}=O$ and water. When using PMSO as a molecular probe to detect $Fe^{IV}=O$, Jiang et al.[39] found that, when ^{16}O-PMS and $H_2{}^{18}O$ are employed, the oxidation of PMS^{16}O by $Fe^{IV}=O$ results in the formation of

https://doi.org/10.1038/s41467-025-64318-w

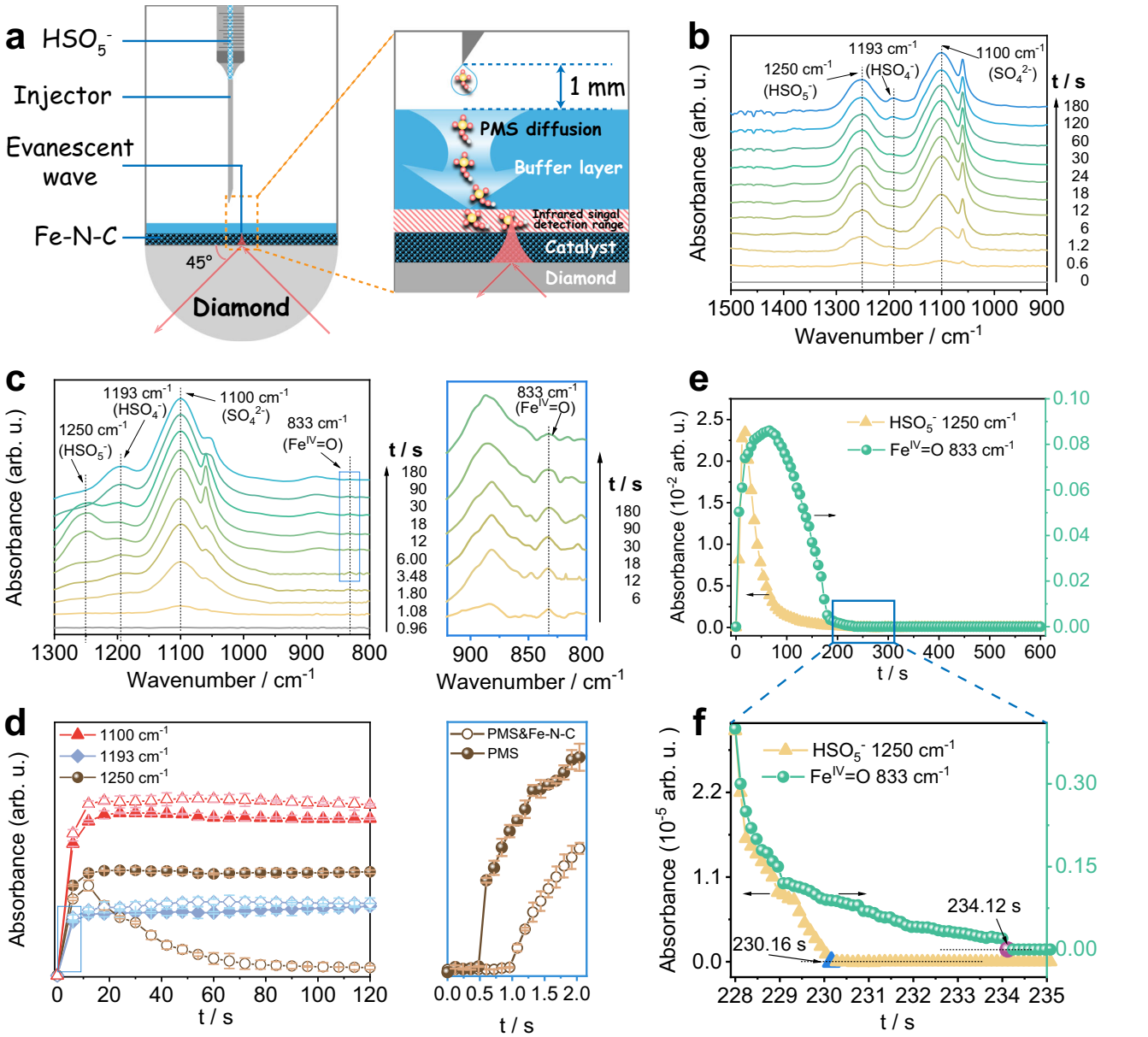

Fig. 3 | PMS diffusion and reaction dynamics on bare and Fe-N-C-loaded ATR crystals. a Schematic illustration of PMS diffusion and reaction in the ATR-IR chamber. **b** Time-dependent IR spectra collected on a bare diamond ATR crystal, showing PMS diffusion without reaction. **c** Time-dependent IR spectra collected on an Fe-N-C loaded ATR crystal, capturing both PMS diffusion and reaction. The right panel highlights the $Fe^{IV}=O$ band in an enlarged IR region. **d** Kinetics of HSO_5^- (1250 cm^{-1}), HSO_4^- (1193 cm^{-1}) and SO_4^{2-} (1100 cm^{-1}) growth derived from time-dependent spectra. Solid symbols represent the bare diamond case, while empty symbols correspond to the Fe-N-C-loaded diamond. The inset zooms in on the time region from 0 to 2 s. **e** Kinetics for the growth and decay of HSO_5^- (1250 cm^{-1}) and $Fe^{IV}=O$ (833 cm^{-1}) on the Fe-N-C loaded diamond. **f** Enlarged view of the time region from 228 to 236 s for more specific details of the degradation. The error bars in Fig. 3d are based on data from at least three parallel experiments. Source data for Fig. 3b–f are provided as a Source Data file.

mixed-labeled $PMS^{16}O^{18}O$. This observation raises the possibility that following the formation of $Fe^{IV}={}^{16}O$ from ^{16}O-PMS, an oxygen exchange with $H_2{}^{18}O$ may lead to the formation of $Fe^{IV}={}^{18}O$ and the subsequent oxidation products of $PMS^{16}O^{18}O$ (Fig. 4a).

Interestingly, as shown in Fig. 4b, in the IR spectra, replacing regular $H_2{}^{16}O$ with $H_2{}^{18}O$ revealed a new band at 795 cm^{-1}. The original 833 cm^{-1} band persisted in the early stages of the reaction, but with decreased intensity compared to the scenario with only ^{16}O. As the reaction progressed, the 833 cm^{-1} band gradually diminished, leaving the 795 cm^{-1} band as the sole observed feature. The theoretical value for the $^{18}O/^{16}O$ isotope shift can be predicted using vibration frequency calculation equations ("Isotope shift calculation" section in Supplementary Information). If the 833 cm^{-1} band is assigned to $Fe=^{16}O$, its ^{18}O counterpart should shift down to 796 cm^{-1}, closely aligning with the observed band at 795 cm^{-1}. Literature also supports a theoretical shift of approximately 36 cm^{-1} for the Fe-O harmonic oscillator[17,40]. We also performed a control experiment mixing regular ^{16}O-PMS with $H_2{}^{18}O$ to check for the presence of ^{18}O-persulfate through oxygen exchange (Supplementary Fig. 9a). However, no isotope-shifted band for persulfate was observed in the IR spectra, indicating that direct oxygen exchange does not occur between PMS and H_2O. In addition, we dissolved ^{16}O-labeled PMS in $H_2{}^{18}O$ and allowed the solution to stand for 24 h. High-resolution mass spectrometry (HRMS, Supplementary Fig. 9b) was then performed, and no peak corresponding to ^{18}O-labeled PMS (m/z = 114.96) was detected, thereby ruling out the possibility of oxygen exchange under these conditions. Based on both infrared spectroscopy and high-resolution mass

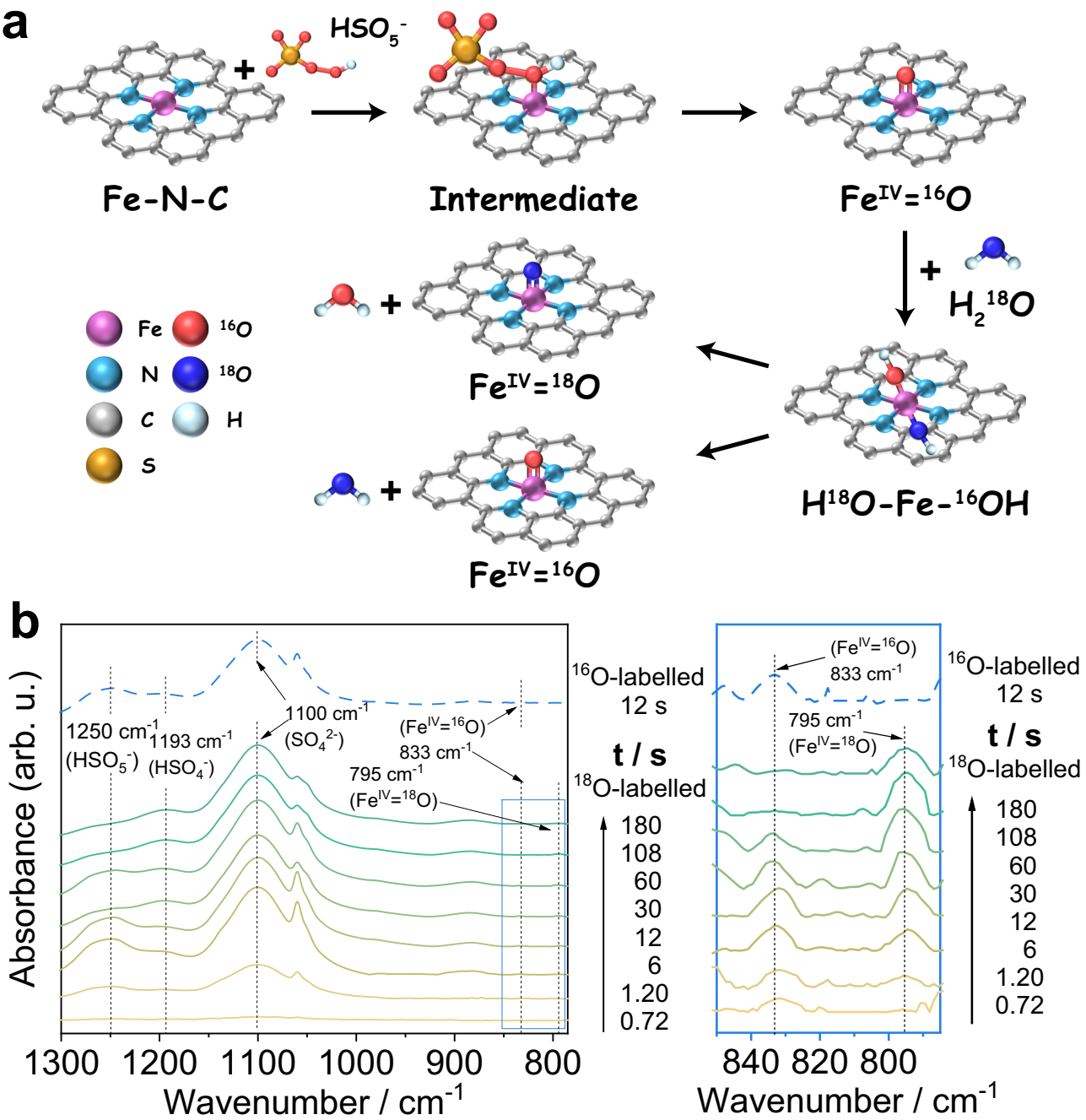

Fig. 4 | Oxygen exchange mechanism between $Fe^{IV}=O$ and water. a Schematic illustration for the oxygen exchange between $Fe^{IV}=O$ and water. **b** Time-dependent IR spectra conducted with ^{16}O-PMS and $H_2{}^{18}O$, the dashed curve exhibits a comparison with ^{16}O-PMS and $H_2{}^{16}O$ (copied from Fig. 3c). The right panel highlights the $Fe^{IV}={}^{16}O$ and $Fe^{IV}={}^{18}O$ bands in an enlarged IR region. Source data for Fig. 4b is provided as a Source Data file.

spectrometry analyses, we can confidently exclude the possibility of oxygen exchange between $H_2{}^{18}O$ and PMS.

Therefore, the observed 795 cm^{-1} band can be assigned to ^{18}O-labelled $Fe^{IV}={}^{18}O$, resulting from an immediate O-exchange between $Fe^{IV}={}^{16}O$ (produced from the oxidation by ^{16}O-persulfate) and $H_2{}^{18}O$. Notably, the growth of the $Fe^{IV}={}^{18}O$ signal exhibited a delayed kinetic profile compared to $Fe^{IV}={}^{16}O$. Since the direct exchange of the oxo-O in a metal-oxo double bond is generally challenging, this kinetic delay would suggest a gradual oxygen-exchange pathway: it resembles the O-exchange between water and the carbonyl group of aldehyde or ketone, which occurs via the formation of a geminal diol intermediate[41–43]. The addition of $H_2{}^{18}O$ on $Fe^{IV}={}^{16}O$ generates a geminal-hydroxyl structure of $Fe^{IV}(^{16}OH)(^{18}OH)$, subsequent dehydration of this intermediate yields either $Fe^{IV}={}^{18}O$ or reverts to $Fe^{IV}={}^{16}O$, due to the relatively small energy difference between the Fe-^{18}O-H and Fe-^{16}O-H bonds. As a result, multiple exchange cycles are needed to accumulate a significant amount of the $Fe^{IV}={}^{18}O$ species. This requirement for repeated exchange events explains why the $Fe^{IV}={}^{18}O$ signal does not emerge with the same kinetics as $Fe^{IV}={}^{16}O$, and instead appears with a noticeable delay. Nevertheless, this isotope experiment further supports our assignment of the 833 cm^{-1} band to surface $Fe^{IV}=O$. More importantly, the observed oxygen exchange indicates that this surface $Fe^{IV}=O$ species possesses a relatively long lifetime and stability in the aqueous matrix, making it a potentially high-activity species for degrading aqueous pollutants.

https://doi.org/10.1038/s41467-025-64318-w

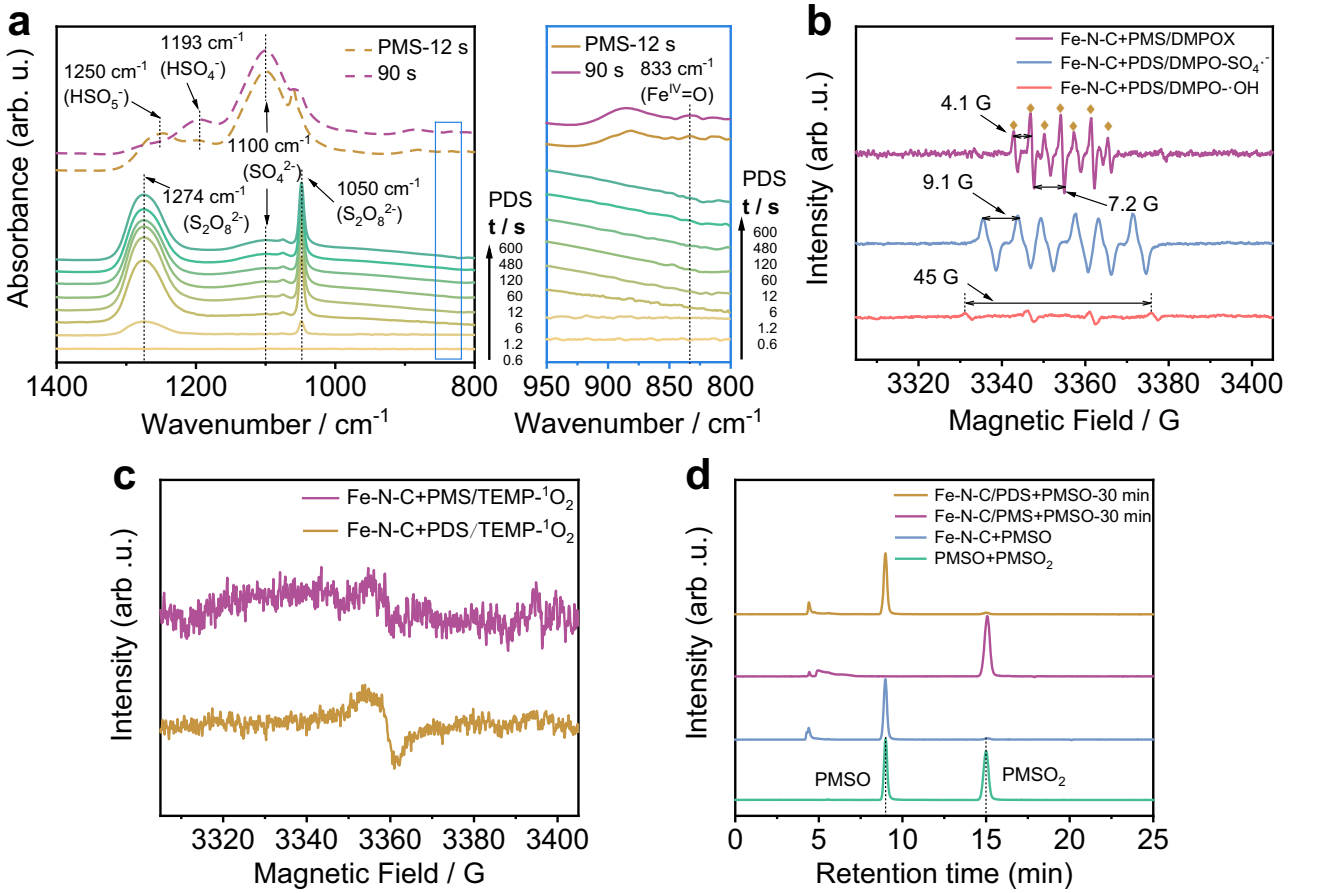

Fig. 5 | Comparative spectroscopic identification of reactive species in PMS and PDS systems. a Time-dependent IR spectra conducted with ^{16}O-PDS and $H_2{}^{16}O$, the dashed curve exhibited comparison with ^{16}O-PMS and $H_2{}^{16}O$ (copied from Fig. 3c). The right panel highlights the $Fe^{IV}=O$ band in an enlarged IR region. To improve the clarity of the spectral features and facilitate better observation of $Fe^{IV}=O$ related signals, we have replaced the dashed lines with solid lines in the relevant figures. **b** The detection of reactive radicals in EPR spectra using 5,5-dimethyl-1-pyrrolidine-N-oxide (DMPO) as a trapping agent. **c** The EPR spectra using 2,2,6,6-tetramethyl-4-piperidinyloxyl (TEMP) as a trapping agent. **d** The high performance liquid chromatography (HPLC) absorption spectra for PMSO oxidation and $PMSO_2$ generation. Source data for Fig. 5a–d are provided as a Source Data file.

The dynamic spectroscopic identification of $Fe^{IV}=O$ in the Fenton-like reaction between Fe-N-C and PDS

For comparison, we performed similar experiments with the replacement of PMS with peroxydisulfate (PDS), using the same SF-ATR-FTIR characterization method (Fig. 5a). Unlike PMS, commercial-available PDS is a pure sample that exhibits characteristic IR peaks at 1274 cm^{-1} and 1050 cm^{-1}, corresponding to the SO_4 moiety in the $S_2O_8^{2-}$ group (Supplementary Fig. 10a). During the in-situ monitoring the Fenton reaction between PDS and Fe-N-C, as shown in Fig. 5a, the appearance of PDS peaks exhibited a similar delay owing to PDS diffusion. The kinetic behavior mirrored that of PMS, initially increasing, reaching a maximum, and then declining to extinction. We also observed the growth of SO_4^{2-} and HSO_4^- peaks, demonstrating a reaction between PDS and Fe-N-C. However, no new characteristic peaks were observed in the 800 ~ 900 cm^{-1} range. Replacing $H_2{}^{16}O$ with $H_2{}^{18}O$ did not change the characteristic peaks of PDS, and no new characteristic peaks emerged (Supplementary Fig. 10b). Therefore, no $Fe^{IV}=O$ species is produced in the PDS and Fe-N-C system.

To bolster the credibility of our IR findings, we conducted additional analyses using electron paramagnetic resonance (EPR) and PMSO molecular probe experiments. In EPR analysis (Fig. 5b), using 5,5-dimethyl-1-pyrrolidine-N-oxide (DMPO) as a trapping agent, in the PDS system, the intense signal with the typical feature of trapped $SO_4{\bullet}^-$ and •OH can be clearly observed, confirming the generation of $SO_4{\bullet}^-$ and •OH in PDS system. In contrast, these trapped radical signals were absent in the PMS system; instead, we detected the 5,5-dimethyl-2-pyrrolidinone-yloxy (DMPOX; $a_N = 7.2$ G and $a_H = 4.1$ G) signal, an oxidation product of DMPO[44]. The absence of significant signals for trapped $SO_4{\bullet}^-$ and •OH suggests the single-electron oxidation of Fe^{II} to Fe^{III} is negligible in the PMS system, where this pathway is accompanied by the stoichiometric generation of $SO_4{\bullet}^-$ and •OH. Also, for both systems, the absence of $^1O_2$ was also confirmed (Fig. 5c). These results confirm that the PMS and PDS systems generate distinct oxidative species, with the PMS system predominantly producing $Fe^{IV}=O$ directly.

Furthermore, the PMSO molecular probe experiment was performed. As shown in Fig. 5d, the results revealed that PMSO was selectively oxidized to $PMSO_2$ in the Fe-N-C/PMS system, whereas no $PMSO_2$ signal was detected in the Fe-N-C/PDS system. Given that $Fe^{IV}=O$ is known to selectively oxidize PMSO to $PMSO_2$, whereas •OH and $SO_4{\bullet}^-$ cannot, these findings are consistent with the IR and EPR results, confirming the formation of $Fe^{IV}=O$ species in the PMS system and suggesting their absence in the PDS system

Combining the results from in-situ FT-IR and EPR, we conclude that PMS effectively activates Fe-N-C, resulting in the formation of surface $Fe^{IV}=O$ species as the dominant active species. In contrast, the presence of PDS primarily generates free radicals such as $SO_4{\bullet}^-$ and •OH, with no detectable $Fe^{IV}=O$ formation. To elucidate the mechanistic differences between the PMS and PDS systems, we performed density functional theory (DFT) calculations with a focus on the detailed reaction intermediates and transition states, aiming to clarify the disparity in energy barriers between the two pathways. Our

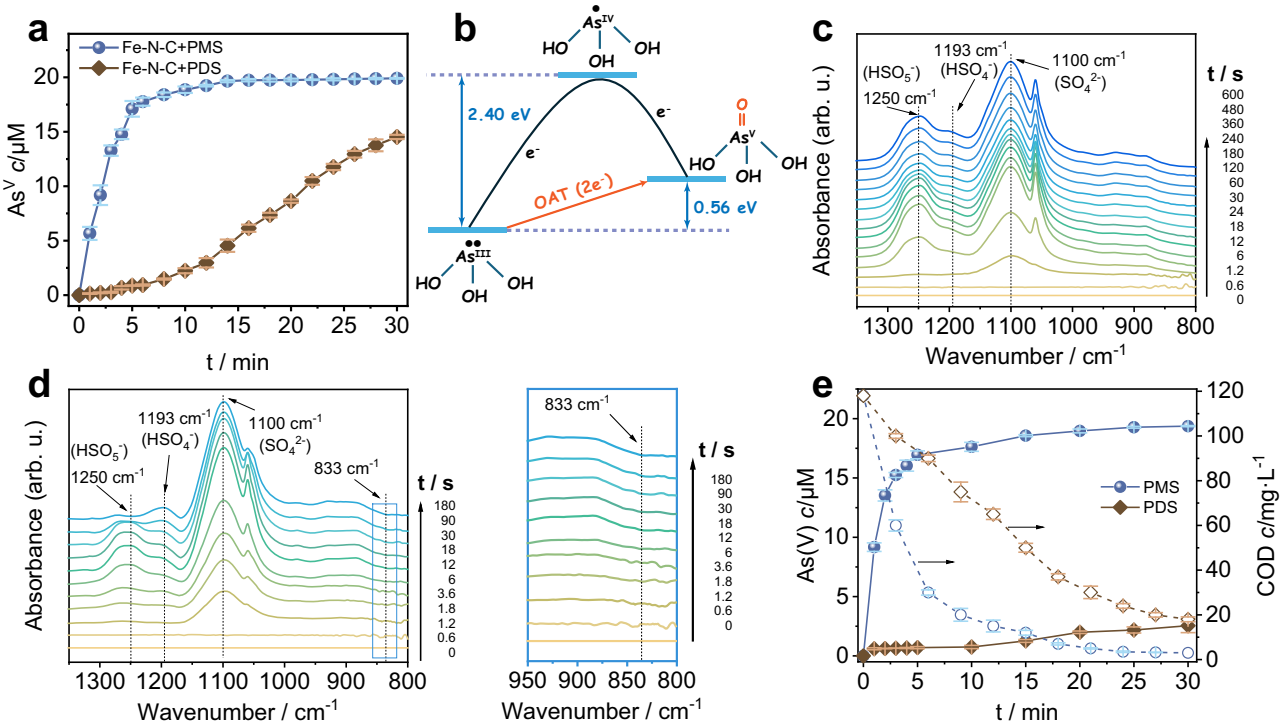

Fig. 6 | Evaluation of As^{III} oxidation performance and mechanism in different water matrices using Fe-N-C-based catalytic systems. a Variation in As^{V} concentration during the oxidation of As^{III} in a deionized water matrix using PMS/Fe-N-C and PDS/Fe-N-C (the complete data in Supplementary Table 2). **b** Schematic diagram illustrating the energy barrier for the one-electron oxidation of As^{III} to As^{IV} and the direct oxygen atom transfer process. **c** Time-dependent IR spectra collected on a bare diamond ATR crystal in As^{III} buffer solution, showing PMS diffusion without reaction. **d** The time-dependent IR spectra of As^{III} oxidation by Fe-N-C/PMS, simultaneously capturing the diffusion and reaction of PMS. The right panel presents a magnified infrared region highlighting the $Fe^{IV}=O$ band. **e** Variation of As^{V} concentration (solid line) and chemical oxygen demand (COD) (dashed line) during the removal of As^{III} in a real lake water matrix (the complete data in Supplementary Table 3). The error bars in Fig. 6a and e are based on data from at least three parallel experiments. Experimental conditions for As^{III} removal in panels (a) and (e): [As^{III}] = 20 μM; [PMS] or [PDS] = 50 μM; [Fe-N-C] = 50 mg·L^{-1}. Source data for Fig. 6a, c-e are provided as a Source Data file.

calculations revealed that the PMS system facilitates the rapid formation of the high-valent $Fe^{IV}=O$ species via a low-barrier oxygen atom transfer (OAT) process, with an overall activation free energy of 13.5 kcal/mol (Supplementary Fig. 11, Supplementary Data 1). In contrast, the PDS system follows a distinct single electron transfer (SET) mechanism. Although the initial step is highly exergonic, then owing to the more complex dimeric structure of PDS compared to PMS, the formation of $Fe^{IV}=O$ by PDS then requires involving multiple intermediates and transition states. The cumulative effect of these steps results in a significantly higher overall energy barrier along the reaction coordinate, making the formation of $Fe^{IV}=O$ in the PDS system both not only thermodynamically and kinetically unfavorable (Supplementary Fig. 12, Supplementary Data 1). As a result, the $Fe^{IV}=O$ species is effectively inaccessible under PDS conditions.

To further demonstrate the universality and reliability of our SF-ATR-FTIR technique in identifying $Fe^{IV}=O$ species, we synthesized two additional Fe-N_x-based single-atom catalysts (Supplementary Fig. 13; Supplementary Table 4). During in situ monitoring of their Fenton-like reactions, a characteristic IR band around 830 cm^{-1} was consistently observed for both catalysts (Supplementary Fig. 14a, b). Complementary PMSO molecular probe experiments and EPR analyses also supported the presence of $Fe^{IV}=O$. These consistent findings confirmed that the ~830 cm^{-1} IR band detected by our technique is a reliable indicator of $Fe^{IV}=O$ formation (Supplementary Fig. 14c–e).

Practical application of $Fe^{IV}=O$ as an oxygen transfer reagent

$Fe^{IV}=O$ has been recognized for its ability to facilitate an oxygen-atom transfer (OAT) process during the oxidation of organic and inorganic substrates[18]. This characteristic makes it especially effective in oxidizing substrates that possess lone-pair electrons, for instance, the aqueous arsenic (III) (As^{III}). The aqueous As^{III}, classified as a Group I carcinogen by the International Agency for Research on Cancer (IARC), has garnered significant attention due to its health risks[45], even low-level exposure to As^{III} can lead to various health issues. The preferred approach to remove As^{III} is to oxidize it to arsenate (As^{V}), which has lower toxicity and is more readily removed by physical-chemical methods[46]. However, a significant challenge is that, in a real environmental system, aqueous As^{III} typically exists at low concentrations and coexists with large amounts of low-toxicity organic and inorganic substrates. This presence complicates the use of broad-spectrum oxidizing agents, like radicals, which cannot selectively oxidize As^{III} in the presence of interfering substrates.

We first assessed the effectiveness of the Fe-N-C/PMS system for removing 20 μM As^{III} in a deionized water matrix. By quantifying the produced As^{V} (Supplementary Fig. 15), we found a significant generation of As^{V} within just 5 min, with approximately 85.5% of As^{III} rapidly converted to As^{V} during this time (Fig. 6a). The final degradation rate of As^{III} reached 99.55% within 15 min, demonstrating the high efficiency of the Fe-N-C/PMS system in treating As^{III}. In contrast, when using the Fe-N-C/PDS system, where the ROS shifted from $Fe^{IV}=O$ to free radicals, only trace amounts of As^{V} were detected in the initial 5 min, after which the generation of As^{V} became more pronounced. A scaled-up As^{III} removal experiment (Supplementary Fig. 16) was also conducted to demonstrate the feasibility of Fe-N-C/PMS even in the enlarged system. In addition, we re-collected the Fe-N-C catalyst (Fe-N-C-r) after the As^{III} degradation experiment and performed a series of post-reaction characterizations, including EXAFS, XPS, and HAADF-STEM (Supplementary Fig. 17), to verify the stability of the catalyst. The superior performance of Fe-N-C/PMS in the oxidative removal of As^{III} can be attributed to the differing mechanisms. As shown in Fig. 6b, in

the Fe-N-C/PDS system, the predominant radicals, with •OH and SO_4•$^-$, initiate a one-electron oxidation process that first converts As^{III} to As^{IV}, this one-electron oxidation step faces a significant energy barrier of 2.40 eV, which slows the reaction in the initial stage. As a result, only a limited amount of As^{V} is generated until most As^{III} is oxidized to As^{IV}. Once this occurs, the oxidation of As^{IV} to As^{V} becomes energetically favorable, leading to an increase in As^{V} production as observed in Fig. 6a. In contrast, in the Fe-N-C/PMS system, the dominant ROS, Fe^{IV} = O, facilitates a more efficient two-electron oxygen-atom transfer that directly transforms As^{III} to As^{V} with a much lower energy barrier of only 0.56 eV. This mechanism results in more efficient oxidative removal of As^{III}. The specific reactivity of Fe^{IV} = O in As^{III} oxidation was also confirmed by our ST-ATR-FTIR measurements. First, the direct reaction between free PMS and As^{III} was excluded by the control experiment in the absence of the Fe-N-C catalyst, as the introduction of As^{III} did not cause any decay in the characteristic peak of PMS at 1250 cm^{-1} within 10 min' reaction (Fig. 6c). Subsequently, when the Fe-N-C catalyst was immobilized on the ATR surface, co-injection of As^{III} and PMS led to the disappearance of the Fe^{IV} = O characteristic band at 833 cm^{-1}, indicating its rapid consumption by As^{III} (Fig. 6d).

We then assessed the removal of As^{III} in a real lake water matrix, sourced from the artificial lake at Beijing Olympic Park, which had a chemical oxygen demand (COD) value of 118 mg·L^{-1}. Using the Fe-N-C/PMS system, the aqueous contaminants were effectively degraded, resulting in a COD reduction to 3 mg·L^{-1} within 30 min (Fig. 6e). Notably, despite the presence of various interfering contaminants, the removal of As^{III} remained highly effective and a removal ratio of 96.8% was achieved. In contrast, while the Fe-N-C/PDS system also led to a significant decrease in COD, the conversion of As^{III} to As^{V} was substantially hindered compared to the distilled water experiments, with only a small amount of As^{V} detected after 30 min and an As^{III} removal ratio of only 12.5%. Similarly, the presence of humic acid and pH adjustment had minimal impact on As^{III} removal by the Fe-N-C/PMS system, highlighting its excellent resistance to environmental interferences (Supplementary Figs. 18, 19). These results underscore the superior performance of Fe-N-C/PMS in selectively removing As^{III} even in complex wastewater environments. This effectiveness stems from the specific reactivity of Fe^{IV} = O towards As^{III} and the long lifetime of the Fe^{IV} = O species generated in the Fe-N_4 isolated structure. The extended stability of Fe^{IV} = O ensures that the oxidative potential of PMS is utilized efficiently to remove As^{III} and other contaminants, rather than being lost to meaningless decay.

This Fe-N-C/PMS system would demonstrate strong potential for practical environmental remediation owing to its excellent recoverability, cost-efficiency, and compatibility with existing water treatment processes. The catalyst can be recovered through simple physical methods, and future development of floating-type configurations may further improve separation efficiency and operational feasibility. Its unique ability to selectively oxidize As^{III} via the formation of Fe^{IV} = O, combined with the high catalytic efficiency and low metal loading requirements of a single-atom catalyst, significantly reduces material costs. Moreover, PMS is already widely used in advanced oxidation processes, and the Fe-N-C/PMS system enhances both degradation efficiency and selectivity, ensuring seamless integration with current treatment infrastructures. These features collectively position the system as a promising candidate for scalable and sustainable water treatment applications.

Discussion

In summary, with the utilization of a spectrometer-controlled syringe pump, we synchronized the initiation of the Fenton reaction with IR data acquisition, allowing for dynamic monitoring of the heterogeneous Fenton reaction, including the variations and kinetics of reactants and intermediates with millisecond time resolution. This operando technique is not only applicable to Fenton reactions but can also be utilized for other reactions initiated by mixing reactants, offering valuable insights into reaction mechanisms.

With the support of this operando approach, we have advanced our understanding of heterogeneous Fe-oxo species, ROS that exhibit distinct reaction pathways compared to other radical ROS generated in Fenton systems. Our findings not only confirmed the presence of Fe-oxo species in the Fenton reaction but also elucidated their kinetic behaviors. Notably, we provided the experimental evidence of their lifetime on the timescale of seconds in aqueous systems. In contrast to the short-lived •OH or SO_4•$^-$, which last only nanoseconds, the long-lived Fe-oxo species minimize the loss of oxidative equivalents during ROS decay or recombination. This maximizes the oxidative potential of persulfate and other Fenton reagents for pollutant removal. Furthermore, the specific oxygen-atom transfer capabilities of Fe-oxo species make them particularly effective for the preferential removal of aqueous arsenic pollutants, even in complex wastewater environments.

Methods

Catalyst synthesis

Fe-N-C was synthesized following the procedure of Zhang et al.[23,35]. First, 0.5 mmol of $Fe(OAc)_2$ and 1.5 mmol of phen were dissolved in 50 mL of ethanol and sonicated for 10 min. Next, 3.16 g of nano-MgO was added and the mixture was sonicated for another 10 min. The mixture was then stirred and refluxed at 60 °C for 12 h. After refluxing, the ethanol solvent was removed by rotary evaporation, and the remaining solid was dried at 60 °C overnight. The dried solid was then transferred to a tube furnace and calcined in an N_2 atmosphere at 700 °C for 2 h, with a ramp rate of 2 °C per minute. The resulting black solid was dispersed in 100 mL of 1.0 M HNO_3 solution and stirred at room temperature for 2 h. This acid treatment was repeated three times to remove the MgO carrier. The recovered solid was washed with water until the filtrate reached neutral pH, then dried at 60 °C for 12 h to obtain Fe-N-C.

Characterization

The micro-morphology and nanostructure of the catalysts were characterized by field emission scanning electron microscopy (SEM, ZEISS GeminiSEM 300) and transmission electron microscopy (TEM, JEOL JEM-F200), along with energy dispersive X-ray spectroscopy (EDS). X-ray diffraction (XRD) patterns were recorded with a Rigaku D/max 2500 diffractometer using Cu Kα radiation. X-ray photoelectron spectroscopy (XPS) was performed on an ESCALAB250XI instrument. High-angle annular dark field scanning transmission electron microscopy (HAADF-STEM) images were captured using a JEM-ARM300F microscope. Electron paramagnetic resonance (EPR) spectra were obtained with a Bruker Elexsys E500-T spectrometer. In-situ attenuated total reflection Fourier-transform infrared (ATR-FTIR) spectra were collected using a Bruker Vertex70V. UV-visible absorption spectra were measured with a Hitachi UV-visible spectrophotometer (UV-3900).

Sample preparation for SF-ATR-FTIR: Specifically, the Fe-N-C was dispersed in distilled water at a concentration of 2 mg·mL^{-1} to prepare a deposition ink. Then, 10 μL of the ink was dropped onto the ATR crystal and dried in situ using an evacuation line to form a uniform membrane. As a result, approximately 20 μg of Fe-N-C was deposited as a thin film on the ATR crystal for subsequent IR measurements.

Data availability

The raw data for each curve in Figs. 2e, f, 3b–f, 4b, 5a–d, 6a, 6c–e and Supplementary Figs.. generated in this study are provided in the Source Data file. Source data are provided in this paper. All the raw data relevant to the study are available from the corresponding author upon request. Source data are provided with this paper.

References

1. Gao, L. et al. Mechanistic study on the role of soluble microbial products in sulfate radical-mediated degradation of pharmaceuticals. *Environ. Sci. Technol.* **53**, 342–353 (2019).
2. Wang, J. et al. Activation of persulfate (PS) and peroxymonosulfate (PMS) and application for the degradation of emerging contaminants. *Chem. Eng. J.* **334**, 1502–1517 (2018).
3. Huang, M. et al. Facilely tuning the intrinsic catalytic sites of the spinel oxide for peroxymonosulfate activation: From fundamental investigation to pilot-scale demonstration. *Proc. Natl Acad. Sci. Usa.* **119**, e2202682119 (2022).
4. Zhou, Q. et al. Generating dual-active species by triple-atom sites through peroxymonosulfate activation for treating micropollutants in complex water. *Proc. Natl Acad. Sci. Usa.* **120**, e2300085120 (2023).
5. Lee, J., von Gunten, U. & Kim, J. H. Persulfate-based advanced oxidation: critical assessment of opportunities and roadblocks. *Environ. Sci. Technol.* **54**, 3064–3081 (2020).
6. Zhao, Z. et al. Turning the inert element zinc into an active single-atom catalyst for efficient Fenton-like chemistry. *Angew. Chem. Int. Ed.* **62**, e202219178 (2023).
7. Zhang, Y. J. et al. Simultaneous nanocatalytic surface activation of pollutants and oxidants for highly efficient water decontamination. *Nat. Commun.* **13**, 3005 (2022).
8. He, Y. et al. Fe-Mn oxycarbide anchored on N-doped carbon for enhanced Fenton-like catalysis: Importance of high-valent metal-oxo species and singlet oxygen. *Appl. Catal. B-Environ. Energy* **340**, 123204 (2024).
9. Zhang, L. et al. Carbon nitride supported high-loading Fe single-atom catalyst for activation of peroxymonosulfate to generate $^1O_2$ with 100% selectivity. *Angew. Chem. Int. Ed.* **60**, 21751–21755 (2021).
10. Bao, Y. et al. Generating high-valent iron-oxo identical with ≡Fe^{IV}=O complexes in neutral microenvironments through peroxymonosulfate activation by Zn-Fe layered double hydroxides. *Angew. Chem. Int. Ed.* **61**, e202209542 (2022).
11. Chen, T. et al. Robust Fe-N_4-C_6O_2 single atom sites for efficient PMS activation and enhanced Fe^{IV}=O reactivity. *Nat. Commun.* **16**, 2402 (2025).
12. Liu, H. et al. Tailoring d-band center of high-valent metal-oxo species for pollutant removal via complete polymerization. *Nat. Commun.* **15**, 2327 (2024).
13. Song, J. et al. Asymmetrically coordinated CoB_1N_3 moieties for selective generation of high-valence Co-oxo species via coupled electron-proton transfer in fenton-like reactions. *Adv. Mater.* **35**, e2209552 (2023).
14. Zong, Y. et al. Enhanced oxidation of organic contaminants by iron(II)-activated periodate: The significance of high-valent iron–oxo species. *Environ. Sci. Technol.* **55**, 7634–7642 (2021).
15. Ezhov, R., Ravari, A. K. & Pushkar, Y. Characterization of the Fe^{V}=O Complex in the Pathway of Water Oxidation. *Angew. Chem. Int. Ed.* **59**, 13502–13505 (2020).
16. Serrano-Plana, J. et al. Exceedingly Fast Oxygen Atom Transfer to Olefins via a Catalytically Competent Nonheme Iron Species. *Angew. Chem. Int. Ed.* **55**, 6310–6314 (2016).
17. Gordon, J. B. et al. A reactive, photogenerated high-spin (*S*=2) Fe^{IV}(O) complex via O_2 activation. *J. Am. Chem. Soc.* **143**, 21637–21647 (2021).
18. Zhao, Y. et al. -Fe_2O_3 as a versatile and efficient oxygen atom transfer catalyst in combination with H_2O as the oxygen source. *Nat. Catal.* **4**, 684–691 (2021).
19. Avenier, F. et al. Photoassisted generation of a dinuclear Iron(III) peroxo species and oxygen-atom transfer. *Angew. Chem. Int. Ed.* **52**, 3634–3637 (2013).
20. Dan, M. What are the oxidizing intermediates in the Fenton and Fenton-like reactions? A perspective. *Antioxidants* **11**, 1368 (2022).
21. Vijay, A. K. et al. Reaction of Fe_{aq}^{II} with peroxymonosulfate and peroxydisulfate in the presence of bicarbonate: Formation of Fe_{aq}^{IV} and carbonate radical anions. *Environ. Sci. Technol.* **57**, 6743–6753 (2023).
22. Dong, Z. et al. A novel diagnostic method for distinguishing between Fe(IV) and •OH by using atrazine as a probe: Clarifying the nature of reactive intermediates formed by nitrilotriacetic acid assisted Fenton-like reaction. *J. Hazard. Mater.* **417**, 126030 (2021).
23. Cheng, C. et al. Generation of Fe^{IV}=O and its contribution to Fenton-like reactions on a single-atom Iron-N-C catalyst. *Angew. Chem. Int. Ed.* **62**, e202218510 (2023).
24. Lin, Y. et al. Coordination engineering of heterogeneous high-valent Fe(IV)-oxo for safe removal of pollutants via powerful Fenton-like reactions. *Nat. Commun.* **15**, 10032 (2024).
25. Wang, J. et al. Interlayer structure manipulation of iron oxychloride by potassium cation intercalation to steer H_2O_2 activation pathway. *J. Am. Chem. Soc.* **144**, 4294–4299 (2022).
26. Pan, L. et al. Visible light-driven Selective organic degradation by $FeTiO_3$/persulfate system: the formation and effect of high valent Fe(IV). *Appl. Catal. B-Environ. Energy* **280**, 119414 (2021).
27. Mártire, D. O. et al. Kinetic study of the reactions of oxoiron(IV) with aromatic substrates in aqueous solutions.*J. Chem. Kinet.* **34**, 488–494 (2002).
28. Yao, J. et al. Methyl phenyl sulfoxide (PMSO) as a quenching agent for high-valent metal-oxo species in peroxymonosulfate based processes should be reconsidered. *Chem. Eng. J. Adv.* **12**, 100378 (2022).
29. Luong, T. Q. et al. Hydrostatic pressure increases the catalytic activity of amyloid fibril enzymes. *Angew. Chem. Int. Ed.* **55**, 12412–12416 (2016).
30. Kas, R. et al. In-situ infrared spectroscopy applied to the study of the electrocatalytic reduction of CO_2: theory, practice, and challenges. *ChemPhysChem* **20**, 2904–2925 (2019).
31. Chen, F. et al. Single-atom iron anchored tubular g-C_3N_4 catalysts for ultrafast Fenton-like reaction: roles of high-valency iron-oxo species and organic radicals. *Adv. Mater.* **34**, e2202891 (2022).
32. Xiong, Y. et al. Single-atom Fe catalysts for Fenton-like reactions: Roles of different N species. *Adv. Mater.* **34**, 2110653 (2022).
33. Zong, Y. et al. Unraveling the overlooked involvement of high-valent cobalt-oxo species generated from the cobalt(II)-activated peroxymonosulfate process. *Environ. Sci. Technol.* **54**, 16231–16239 (2020).
34. Wang, Q. et al. Degradation of bisphenol a using peroxymonosulfate activated by single-atomic cobalt catalysts: Different reactive species at acidic and alkaline pH. *Chem. Eng. J.* **439**, 135002 (2022).
35. Liu, W. et al. Discriminating catalytically active FeN_x species of atomically dispersed Fe-N-C catalyst for selective oxidation of the C–H bond. *J. Am. Chem. Soc.* **139**, 10790–10798 (2017).
36. Qian, K. et al. Single-atom Fe catalyst outperforms its homogeneous counterpart for activating peroxymonosulfate to achieve effective degradation of organic contaminants. *Environ. Sci. Technol.* **55**, 7034–7043 (2021).
37. Wu, Z. et al. Long-range interactions driving neighboring Fe–N_4 sites in Fenton-like reactions for sustainable water decontamination. *Nat. Commun.* **15**, 7775 (2024).
38. Hou, K. et al. Reactive high-spin iron(IV)-oxo sites through dioxygen activation in a metal–organic framework. *Science* **382**, 547–553 (2023).
39. Wang, Z. et al. Further understanding the involvement of Fe(IV) in peroxydisulfate and peroxymonosulfate activation by Fe(II) for oxidative water treatment. *Chem. Eng. J.* **371**, 842–847 (2019).
40. Warm, K. et al. A pseudotetrahedral terminal oxoiron(IV) complex: mechanistic promiscuity in C-H bond oxidation reactions. *Angew. Chem. Int. Ed.* **60**, 6752–6756 (2021).

41. Kawanishi, Y. et al. Efficient ^{16}O–^{18}O isotope exchange reactions of carbonyl compounds in aqueous organic solvents catalyzed by acidic resin. *Chem. Eng. J.* **167**, 531–535 (2011).
42. Li, W. et al. Atmospherically relevant acrolein–water complexes: spectroscopic evidence of aldehyde hydration and oxygen atom exchange. *Phys. Chem. Chem. Phys.* **21**, 23559–23566 (2019).
43. Li, X. et al. CoN_1O_2 single-atom catalyst for efficient peroxymonosulfate activation and selective cobalt(IV)=O generation. *Angew. Chem. Int. Ed.* **62**, e202303267 (2023).
44. Chen, L. et al. Accurate identification of radicals by in-situ electron paramagnetic resonance in ultraviolet-based homogenous advanced oxidation processes. *Water Res* **221**, 118747 (2022).
45. Chen, M. et al. Simultaneous oxidation and removal of arsenite by Fe(III)/CaO_2 Fenton-like technology. *Water Res* **201**, 117312 (2021).
46. Wang, Z. et al. Selective oxidation of arsenite by peroxymonosulfate with high utilization efficiency of oxidant. *Environ. Sci. Technol.* **48**, 3978–3985 (2014).

Acknowledgements

This work was supported by the National Natural Science Foundation of China (No. 22222609 and 22321004), the National Key Research and Development Program of China (No. 2020YFA0710303) and the CAS Project for Young Scientists in Basic Research (No. YSBR-004).

Author contributions

Q.Z. and H.S. came up with the original idea; H.S., J.-C.Z. and W.-J.S. supervised the project; Q.Z. and Q.H. designed the experiments; Q.Z. performed the experiments; Q.Z., Q.H., Y.-E.X., Z.-Y.Z. and R.D. performed the characterizations; Q.H. and R.D. helped with the data interpretations; Q.Z. and H.S. wrote the manuscript; all authors commented on it.

Competing interests

The authors declare no competing interests.

Additional information

Supplementary information The online version contains supplementary material available at https://doi.org/10.1038/s41467-025-64318-w.

Correspondence and requests for materials should be addressed to Hua Sheng.

Peer review information *Nature Communications* thanks the anonymous reviewer(s) for their contribution to the peer review of this work. A peer review file is available.